



Original Research

Properties of garnet-type $\text{Li}_6\text{La}_3\text{ZrTaO}_{12}$ solid electrolyte films fabricated by aerosol deposition method

Ryoji Inada*, Takayuki Okada, Akihiro Bando, Tomohiro Tojo, Yoji Sakurai

Department of Electrical and Electronic Information Engineering, Toyohashi University of Technology, 1-1 Hibarigaoka, Tempaku-cho, Toyohashi, Aichi 441-8580, Japan

ARTICLE INFO

Keywords:

Lithium-ion
Garnet
Solid electrolyte
Thick film
Aerosol deposition
Ionic conductivity

ABSTRACT

The garnet-type $\text{Li}_6\text{La}_3\text{ZrTaO}_{12}$ (LLZT) solid electrolyte films were fabricated by aerosol deposition (AD) method. Ball-milled LLZT powder with a cubic garnet structure and a particle size of 1–2 μm was used as raw material and deposited directly on a SUS316L or a glass substrate via impact consolidation. As-deposited LLZT film has a cubic garnet structure but contains Li_2CO_3 and $\text{La}_2\text{Zr}_2\text{O}_7$ phases. SEM observation revealed that the film consists of LLZT particles fractured into submicron size. The impurity phase formation during AD process was caused by the local heating by the collision between LLZT particles and deposition surface and reaction with CO_2 . The Li^+ ion conductivity of LLZT film was estimated to be $0.24 \times 10^{-8} \text{ S cm}^{-1}$ at room temperature. Electronic conductivity of LLZT film was confirmed to be around $10^{-12} \text{ S cm}^{-1}$, indicating the dominant Li^+ ion conduction of LLZT film.

1. Introduction

All-solid-state lithium-ion batteries (LiBs) are expected to be one of the next generation of energy storage devices because of their high energy density, high safety and excellent cycle stability [1–4]. The materials used for solid electrolyte must have not only high lithium-ion conductivity above $10^{-3} \text{ S cm}^{-1}$ at room temperature but also possess chemical stability against electrode materials, air and moisture. Although oxide-based SE materials have rather lower conductivity and poor deformability compared to sulfide-based ones, they have other advantages such as their chemical stability and ease of handling.

Among the various oxide-based SE materials, lithium-stuffed garnet-type oxide with the formula of $\text{Li}_7\text{La}_3\text{Zr}_2\text{O}_{12}$ (LLZ) has been widely studied because of its high conductivity above $10^{-4} \text{ S cm}^{-1}$ at room temperature, excellent thermal performance and stability against metallic lithium [5]. LLZ has two different crystal phases, one is the cubic phase and the another is tetragonal one [6–8], but high total (bulk+grain boundary) conductivity at room temperature above $10^{-4} \text{ S cm}^{-1}$ is mostly confirmed in cubic LLZ sintered at high temperature from 1100 °C to 1200 °C in alumina crucible and/or substituted Al_2O_3 [5,9–12]. During the high temperature sintering, Al^{3+} enters from the crucible and/or substituted Al_2O_3 into the LLZ pellet and works as sintering aid. In addition, it has been pointed out that some amount of Al^{3+} enters into LLZ lattice, modifies the Li^+ ion

vacancy concentration and stabilizes the cubic structure [11,12]. Partial substitution of Zr^{4+} by Nb^{5+} [13] or Ta^{5+} [14–18] in LLZ is reported to be effective to stabilize the cubic garnet structure, and their room temperature conductivity was greatly enhanced up to $10^{-3} \text{ S cm}^{-1}$ by optimizing doping level.

Film-shaped solid electrolyte provides low electrical resistance, small size of a device and increasing volumetric energy density for all-solid-state battery. LLZ film fabrication by using pulsed laser deposition (PLD) [19,20], radio-frequency (RF) magnetron sputtering [21] and sol-gel process [22] has been reported, but their room temperature conductivities were in the range of 10^{-7} – $10^{-5} \text{ S cm}^{-1}$, which is nearly two digits lower than sintered LLZ pellets [5–12]. These film fabrication methods are efficient for fabricating uniform film and controlling the film thickness, but in some cases, it is difficult to control elementary composition. Moreover, increasing substrate temperature during deposition and/or post-annealing should be needed to obtain well-crystallized films. Since high temperature treatments may lead to undesired reactions at the interface or uncontrolled diffusion between electrode and solid electrolyte, these methods are not recommended in some cases for fabricating all-solid-state batteries.

Aerosol deposition (AD) has several advantages compared to other conventional thin film deposition methods as mentioned above, including deposition of polycrystalline film without any heat treatments, a fast deposition rate and high adhesion strength with a

Peer review under responsibility of Chinese Materials Research Society.

* Corresponding author.

E-mail address: inada@ee.tut.ac.jp (R. Inada).

<http://dx.doi.org/10.1016/j.pnsc.2017.06.002>

Received 7 November 2016; Received in revised form 29 May 2017; Accepted 2 June 2017

Available online 09 June 2017

1002-0071/© 2017 Chinese Materials Research Society. Published by Elsevier B.V. This is an open access article under the CC BY-NC-ND license (<http://creativecommons.org/licenses/by-nc-nd/4.0/>).

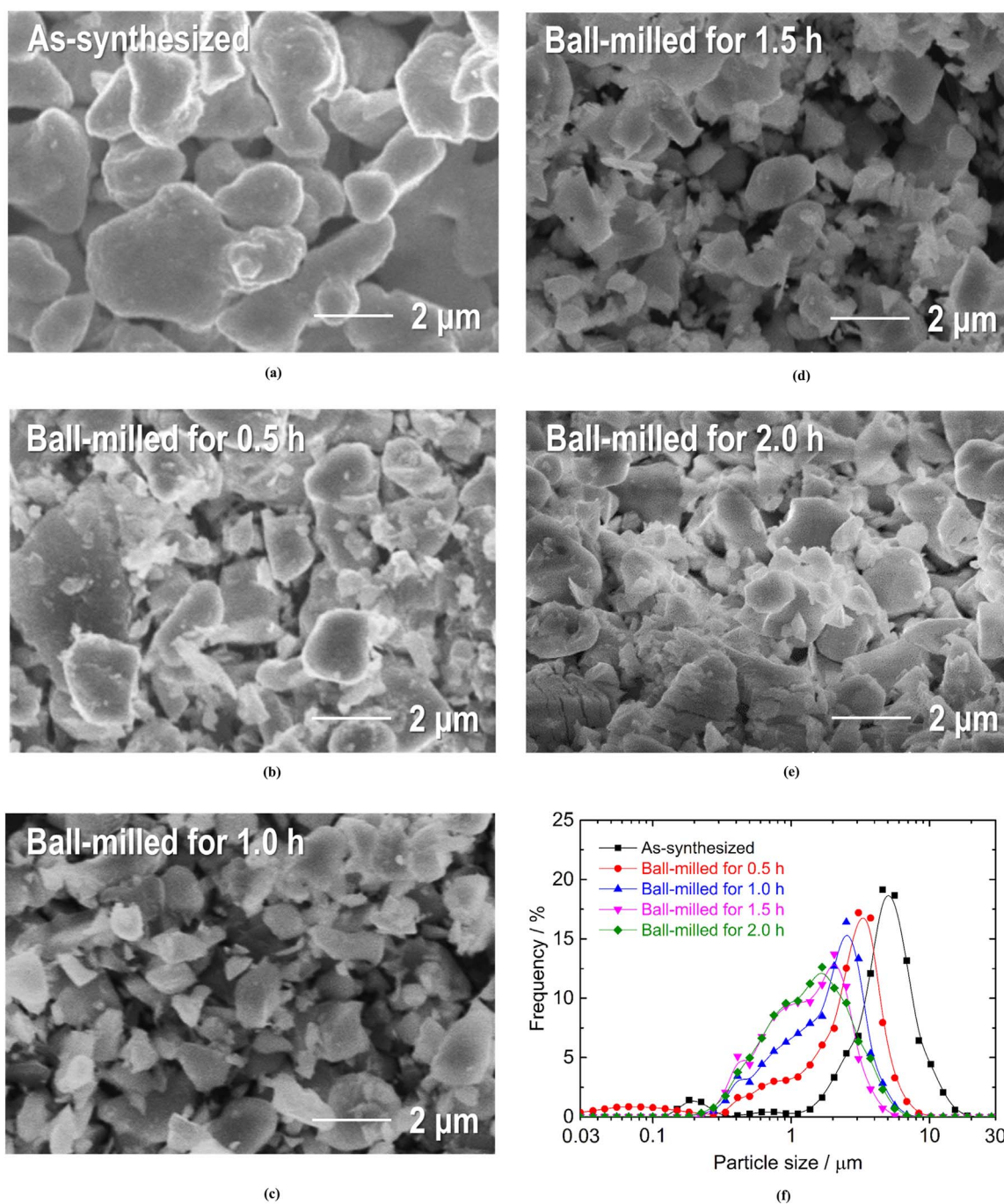


Fig. 1. SEM images of LLZT powders: (a) as-synthesized, (b) ball-milled for 0.5 h and (c) ball-milled for 1.0 h, (d) ball-milled for 1.5 h and (e) ball-milled for 2.0 h. The particle size distributions of all LLZT powders are summarized in (f). The powders (a), (b), (c) and (d) are used for LLZT film fabrication by AD but the film can be formed only using the powder (e).

substrate [23,24]. A film is deposited through impact and adhesion of fine particles on substrate at room temperature. In general, the film fabricated by AD has similar properties with raw powder material, such as crystal structure, composition and physical property. By addressing these attractive features, numerous studies for the film fabrication by AD have been reported in various functional ceramic materials, including $\text{Pb}(\text{Zr},\text{Ti})\text{O}_3$ (PZT) [24], $(\text{K}_{0.5}\text{Na}_{0.5})\text{NbO}_3$ [25] and $\text{Ca}_3\text{Co}_4\text{O}_9$ [26]. Recently, several works have been also reported in the battery field. The electrochemical properties of Si alloy or composite [27], LiMn_2O_4 [28], LiFePO_4 [29], $\text{LiNi}_{1/3}\text{Co}_{1/3}\text{Mn}_{1/3}\text{O}_2$ [30], $\text{Li}_4\text{Ti}_5\text{O}_{12}$ [31], Fe_2O_3 [32] and graphite [33] film electrodes were investigated to verify the feasibility of AD. It has been also reported that AD $\text{Li}_{1+x}\text{Al}_x\text{M}_{2-x}(\text{PO}_4)_3$ ($\text{M} = \text{Ti}, \text{Ge}$) solid electrolyte films with NASICON (Na superionic conductor) structure showed the room

temperature ionic conductivity of 10^{-6} – $10^{-5} \text{ S cm}^{-1}$ [34,35].

Very recently, Ahn et al. reported the properties of LLZ film fabricated by AD, but the conductivity of the film was limited to only $10^{-8} \text{ S cm}^{-1}$ even at 140°C [36]. In their work, Al-doped LLZ powder with a particle size around 7–10 μm is used as raw material and the LLZ film was composed of strongly fractured LLZ nanoparticles with the size of several 10 nm. They have concluded that much lower conductivity than sintered LLZ is mainly attributed to the degradation of crystallinity, significant increase of the volume ratio between grains and grain-boundaries, and possible impurity phase formation in LLZ film due to moisture. However, it is known that both the microstructure and properties of the films fabricated by AD are strongly influenced by the size and the morphology of raw powder materials [31,35], so that the conductivity of LLZ film would be improved by controlling the

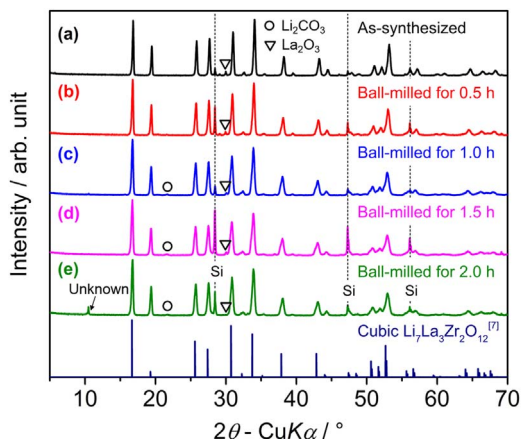


Fig. 2. XRD patterns of LLZT powders: (a) as-synthesized, (b) ball-milled for 0.5 h, (c) ball-milled for 1.0 h, (d) ball-milled for 1.5 h and (e) ball-milled for 2.0 h. Calculated pattern of cubic garnet-type LLZ using crystal structural parameters [7] is also shown.

particle size of raw powder.

In this paper, we fabricated garnet-type $\text{Li}_6\text{La}_3\text{ZrTaO}_{12}$ (LLZT) films by AD, using LLZT powder with a cubic garnet structure and a smaller particle size than the literature [36]. As mentioned above, proper amount of Ta^{5+} substitution into the Zr^{4+} site in LLZ is known to be quite effective to stabilize a cubic garnet structure of LLZ [14–18] and Ta doped LLZ showed not only high conductivity but also high stability against metallic lithium [37–39], so we used Ta substituted LLZ as a raw material for film fabrication by AD. As-synthesized LLZT powder and ball-milled ones with different particle sizes were used as raw material for the film fabrication via impact consolidation. The crystal phases, microstructures and electrical conducting properties of as-deposited LLZT films were investigated.

2. Experimental

Cubic garnet-type LLZT powder was synthesized by a conventional solid state reaction method. Stoichiometric amounts of $\text{LiOH}\cdot\text{H}_2\text{O}$ (Kojundo chemical laboratory, 99%), $\text{La}(\text{OH})_3$ (Kojundo chemical laboratory, 99.99%), ZrO_2 (Kojundo chemical laboratory, 98%) and Ta_2O_5 (Kojundo chemical laboratory, 99.9%) were ground and mixed by planetary ball-milling (Nagao System, Planet M2-3F) with zirconia balls (10 mm in diameter) and ethanol for 3 h, and then calcined at 950 °C for 6 h in a Pt-Au alloy crucible. It is known that both the size and morphology of raw powder are important factors for structure and property of a film fabricated by AD [23,31,35]. In order to prepare LLZT powders with different particle sizes, as-synthesized LLZT powder was pulverized using planetary ball-milling with ethanol and zirconia balls (3 mm in diameter) with different milling time of 0.5, 1.0, 1.5 and 2.0 h. The rotation speed of planetary ball-milling was fixed to 300 rpm. Obtained LLZT powders were used as raw material for fabrication of LLZT film by AD.

Schematic illustration of AD apparatus is reported in the literatures [31,35]. It consists of a carrier gas supply system, an aerosol chamber, a deposition chamber equipped with a motored X–Y–Z stage and a nozzle with a thin rectangular-shaped orifice with a size of 10 mm × 0.5 mm. Deposition starts with evacuating deposition chamber. A pressure difference between carrier gas system and deposition chamber is generated as a power source for film deposition. A carrier gas flows out from gas supply system to aerosol chamber. In aerosol chamber, powder is dispersed into carrier gas with no agglomeration. Finally, well dispersed aerosol flows into deposition chamber through a nozzle and is sprayed onto substrate. Stainless steel SUS316L and glass plates were used as substrates. The deposition area was masked into a square shape with an area size of 10 × 10 mm². Nitrogen (N_2) gas was used as a carrier gas. Deposition chamber was evacuated to a low vacuum state

around 10 Pa and deposition was carried out for 1 h. During deposition process, the stage was moved uni-axially with back-and-forth motion length of 50 mm. The distance between tip of nozzle and substrate was set to be 10 mm. According to our previous study [31,35], mass flow of N_2 carrier gas was fixed to 20 L min⁻¹.

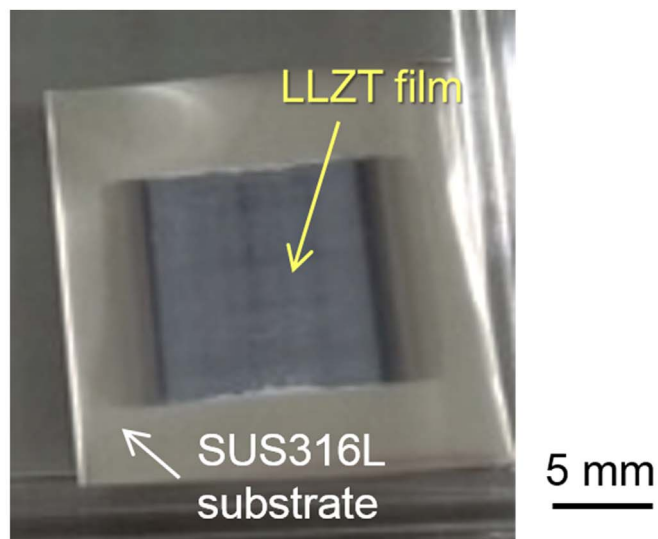
The particle size distributions of LLZT powders were evaluated by using Laser Diffraction Particle Size Analyzer (SALD-2000, Shimadzu). The crystal structure of both raw powder and as-deposited film was evaluated by X-ray Diffractometer (MultiFlex, Rigaku) using $\text{CuK}\alpha$ radiation ($\lambda = 0.15418$ nm), with measurement range $2\theta = 5\text{--}90^\circ$ and step interval of 0.01°. Field emission scanning electron microscope (FE-SEM, SU8000 Type II, Hitachi) was used to observe the morphology and microstructure of both powders and aerosol deposited films. Ionic conductivity of as-deposited LLZT films were evaluated at 27 °C and frequency from 5 Hz to 1 MHz with applied voltage amplitude of 0.1 V, using chemical impedance meter (3532-80, Hioki). Electronic conductivity of both LLZ and LLZT films was evaluated at 27 °C by potentiostatic polarization experiment with an applied voltage of 2 V, using a multichannel potentiostat (VSP-300, Bio-Logic). Before the conductivity measurements, one parallel surface of the LLZ film was sputtered with Au film electrode with an area size of 0.6 × 0.6 cm², so that the film was sandwiched with SUS316L and Au as Li^+ ion blocking electrodes.

3. Results and discussion

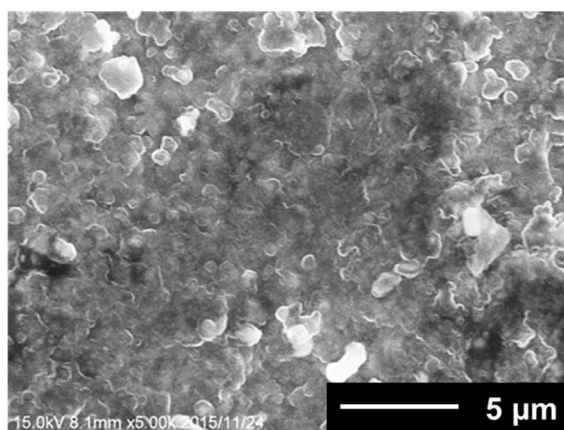
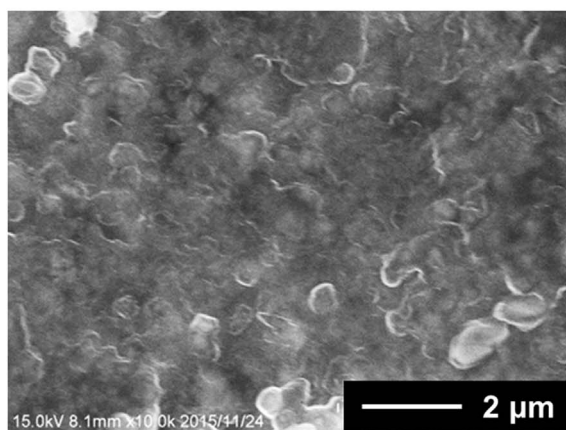
Fig. 1(a)–(e) shows the SEM images of as-synthesized and ball-milled LLZT powders with different milling time. As-synthesized powder dominantly contains LLZT particles with the size around 5 μm and agglomeration among the particles seems to be not remarkable. As shown in Fig. 1(b)–(e), the pulverization of LLZT particles were progressed gradually with increasing the duration times of ball milling, but in the powders milled for 2 h, some small particles were confirmed to be agglomerate. This tendency is corresponding well to the data for the particle size distributions of all LLZT powders summarized in Fig. 1(f). The averaged particle sizes of LLZT powders decreased monotonically with increasing duration time for ball-milling.

XRD patterns for as-synthesized and ball-milled LLZT powders are shown in Fig. 2. For the XRD measurements, Si powder was mixed with all LLZT powders as the reference. The calculated diffraction pattern for cubic garnet-type LLZ with lattice parameter $a = 12.9827$ Å using the structural parameters reported in [7] is also plotted as the reference. As-synthesized LLZT powder has almost a single-phase cubic garnet structure while it contains small amount of La_2O_3 as impurity phases. The all diffraction peaks of as-synthesized powder shift toward higher angle compared with the patterns of LLZ. This is mainly attributed to smaller lattice size of LLZT than LLZ by the substitution of smaller Ta^{5+} (64 pm) into the Zr^{4+} (78 pm) site mentioned in the literatures [14–18]. Ball-milled LLZT powders also have the cubic-garnet structure and the peak position is nearly identical with as-synthesized one, but the diffraction peaks from cubic garnet phase become broader with increasing the milling time from 0.5 to 2.0 h, which is mainly attributed to the degradation of crystallinity of LLZT by mechanical damage during ball-milling. In addition, very small amount of Li_2CO_3 was detected in the ball-milled powders with milling time above 1.0 h and the powder milled for 2.0 h also contained an unknown phase. Li_2CO_3 contained in ball-milled LLZT powder is expected to be formed by the reaction between CO_2 in air and LLZT at the surface of the particles during the processing. In order to suppress the impurity phase formation during ball-milling process and improve the powder quality, it is prefer to control the particle size of as-synthesized powder suitable for film fabrication by AD. Use of sol-gel synthesis method may be a possible way to control the particle size of as-synthesized LLZT powder without impurity phase formation in post powder treatment [40].

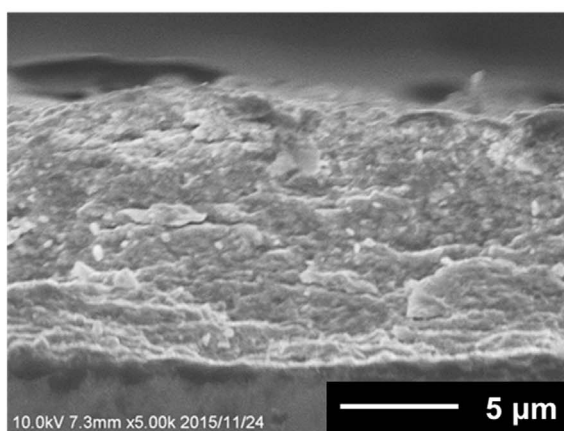
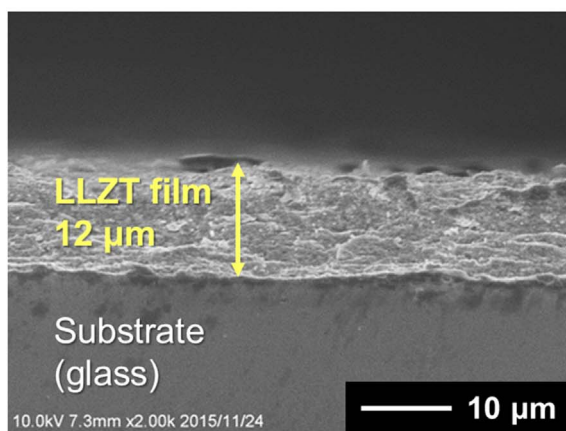
We used the as-synthesized LLZT powder and ball-milled ones with



(a)



(b)



(c)

Fig. 3. (a) A photo of LLZT film formed on a SUS316L substrate. SEM images of a surface and a cross section for LLZT film formed on a glass substrate are shown in (b) and (c).

the milling time of 0.5, 1.0 and 1.5 h for the fabrication of LLZT film by AD, but the film was formed via impact consolidation only using the LLZT powder milled for 1.5 h as raw material. The deposition condition to form LLZT film using 0.5 and 1.0 h milled powder was not clear at present. Comparing with the LLZT powders milled for 0.5 and 1.0 h,

the powder milled for 1.5 h contains many 1–2 μm-sized particles. It is expected that the LLZT particles with the size of 1–2 μm mainly contribute to form LLZT film via impact consolidation. Fig. 3(a) shows the photo of the LLZT film formed on a SUS316L substrate, and Fig. 3(b) and (c) are the SEM images of the surface and the cross-

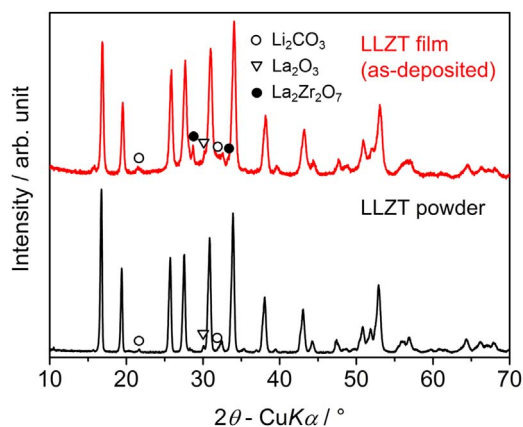


Fig. 4. Comparison of XRD patterns for LLZT film formed on a SUS316L substrate by AD and LLZT powder used for fabrication of the film.

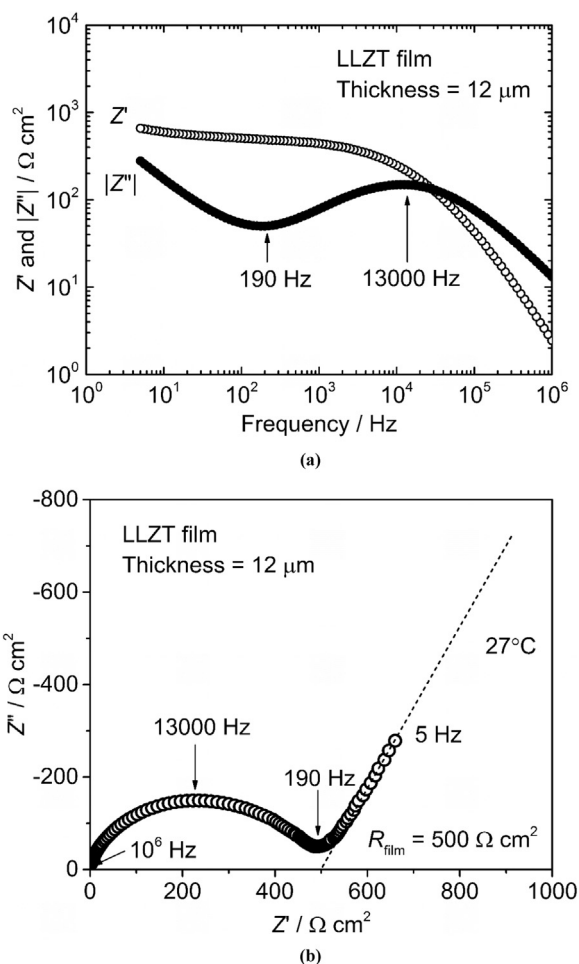


Fig. 5. (a) Bode plot and (b) Nyquist plot of AC impedance measured at 27 °C and 5–10⁶ Hz for LLZT film fabricated by AD.

section of LLZT films formed on a glass substrate. As can be seen, raw LLZT particles are strongly deformed and fractured into the particles with the size far below 1 μm during AD process and they are solidified to form dense polycrystalline film without applying any heat treatments. It is worth noting that the particle size in our LLZT film fabricated by AD seems to be approximately one digit larger than LLZ film reported in [36], which would be mainly attributed to the difference in the particle size of raw LLZ powder. The averaged film thicknesses reached to 12 μm at the deposition time of 1 h, so that the

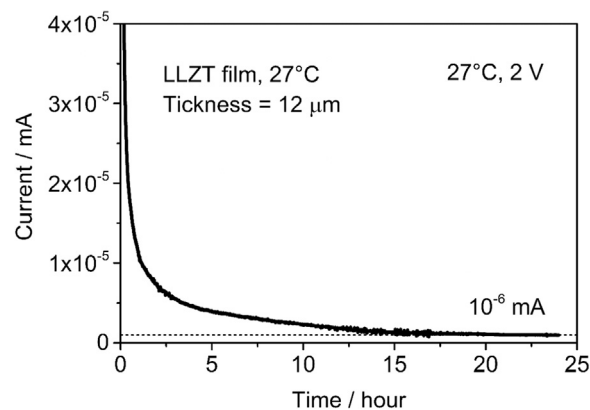


Fig. 6. Potentiostatic polarization current as a function of measuring time at 27 °C and 2 V for LLZT film fabricated by AD.

deposition speed (for deposition areas = 5 cm²) of the film is 0.2 μm min⁻¹.

XRD patterns for the LLZT powder and the LLZT film formed on SUS316L substrate by AD are compared in Fig. 4. It is evident that LLZT film has a cubic garnet structure similar as raw LLZT powder, but the diffraction peaks for the film become broader than those for the powder. Moreover, it is worth noting that the intensity of diffraction peaks from cubic garnet phase in the film is 70% lower than the low powder. This would be caused by the degradation of the crystallinity of LLZT by plastic deformation and/or fracturing of original LLZT powder during the film formation. Similar phenomenon has been confirmed in other ceramic films fabricated by AD [24–26,34,35]. Moreover, Li₂CO₃, La₂O₃ and La₂Zr₂O₇ are contained in the film, and La₂Zr₂O₇ is newly formed during the film fabrication. Such impurity phase formation during AD process has not been observed in the cases for LiFePO₄, [29], LiNi_{1/3}Co_{1/3}Mn_{1/3}O₂ [30], Li₄Ti₅O₁₂ [31] and Li_{1+x}Al_xM_{2-x}(PO₄)₃ (M = Ti, Ge) films [34,35]. In the previous work for LLZ film fabricated by AD [36], the peak intensity of cubic garnet phase of the film is very weak mainly due to strong fracturing of LLZ particles and degradation of crystallinity, so the formation of impurity phases are hard to confirm and have not been discussed in details.

It has been reported that during AD process, the local temperature of the deposition surface is rapidly heated at 200–300 °C by the collision between aerosolized ceramic particles and deposition surface [24]. This local heating would affect the formation of impurity phase in LLZT film formed via impact consolidation. In order to check the temperature increase during AD process, we preliminary fabricated the LLZ film by AD using tetragonal garnet-type LLZ powder as raw material, because the tetragonal LLZ phase is absorbed CO₂ and transformed easily to the cubic phase at temperature from 100 to 400 °C [8,41]. As shown in Fig. S1 in the Supplementary data, the XRD measurement results of as-deposited LLZ film made from tetragonal LLZ powder shows cubic garnet-type diffraction patterns, and Li₂ZrO₃ and La₂Zr₂O₇ are formed during the film formation by impact consolidation. Both the transition from tetragonal phase to cubic one and the impurity phase formation were simultaneously occurred during AD process, so we believe that the local heating at the deposition surface definitely occurred during AD process and it caused the formation of La₂Zr₂O₇ phase. Although the mechanism for the formation of La₂Zr₂O₇ phase during AD process has not been fully clarified at present, small amount of Li contained in LLZ reacted with CO₂ to form Li₂CO₃ and this Li loss in LLZ resulted in the formation of La₂Zr₂O₇ phase.

Li⁺ ion conductivity σ_i of as-deposited LLZT film was measured by AC impedance spectroscopy. Bode plot and Nyquist plot of AC impedance measured at 27 °C for LLZT film is shown in Fig. 5(a) and (b). Here, Z' and Z'' are real and imaginary parts of impedance, and the units of both Z' and Z'' are shown as area specific values. As can

be seen in Fig. 5(b), a semicircle at frequency range from 190 Hz to 10^6 Hz and a linear portion data at below 190 Hz were obtained, suggesting that the conducting nature of the film is primary ionic. Intercept point of linear tail in low frequency range with real axis nearly corresponds to film resistance R_{film} due to ionic conduction, but the quantitative separation of bulk and grain-boundary contribution on R_{film} is difficult. σ_i of LLZT film can be calculated by R_{film} ($= 500 \Omega \text{ cm}^2$) and the film thickness ($= 15 \mu\text{m}$). Consequently, we obtained $\sigma_i = 0.24 \times 10^{-5} \text{ S cm}^{-1}$ at 27°C . σ_i of our LLZT film fabricated by AD are comparable with those for the films fabricated by other film deposition methods such as PLD [19,20], RF magnetron sputtering [21] and sol-gel method [22], and much superior to LLZ film fabricated by AD reported in [36]. However, it is still two digits lower than LLZT with a same composition sintered at high temperature [14,18]. The smaller grain size and the presence of impurity phases such as Li_2CO_3 , La_2O_3 and $\text{La}_2\text{Zr}_2\text{O}_7$ in LLZT films would cause the increase of the grain-boundary resistance for Li^+ ion conduction. Moreover, the bulk Li^+ ion conductivity of LLZT particles consisting the film would be deteriorated by the degradation of crystallinity during the AD process. These two factors are considered as the possible reasons for low conductivity of LLZT film fabricated by AD, but it is not clarified that which factor is dominant at present. Further study should be needed to suppress the formation of the impurity phases in Li-stuffed garnet oxide solid electrolyte film particularly by the powder treatment such as the composition, synthesis route, and controlling of the particle size in future.

Finally, potentiostatic polarization measurement of LLZT film was made to investigate the electron conduction contribution, and the result is shown in Fig. 6. Since we used SUS316L and Au as Li^+ ion blocking electrodes for the measurement, the steady state current in Fig. 6 is attributed to electronic conduction in the film. Electronic conductivity σ_e can be determined from applied DC voltage ($= 2 \text{ V}$), steady state current ($= 10^{-9} \text{ A}$) and geometrical parameters (area of Au-electrode and film thickness). Consequently, σ_e for LLZ film are estimated to be $1.7 \times 10^{-12} \text{ S cm}^{-1}$ at 27°C , which is approximately six digits of magnitude lower than σ_i and sufficient to ensure low self-discharge rate in all-solid-state LiB constructed by using these electrolyte films [34]. This result demonstrates the dominant Li^+ ion conduction of LLZT film.

4. Conclusion

Garnet-type LLZT solid electrolyte film has been fabricated by AD. Ball-milled LLZT powder with a particle size of $1\text{--}2 \mu\text{m}$ is confirmed to be suitable for the fabrication of LLZT film on a stainless steel or a glass substrate via impact consolidation. X-ray diffraction patterns reveals that as-deposited LLZT film has a cubic garnet structure similar as raw LLZT powder, but small amount of impurity phases such as Li_2CO_3 , La_2O_3 and $\text{La}_2\text{Zr}_2\text{O}_7$ are contained. SEM observation reveals that the film consists of LLZ particles fractured into submicron size. The Li^+ ion conductivity of LLZT film is estimated to be $0.24 \times 10^{-5} \text{ S cm}^{-1}$ at 27°C , which is approximately two digits lower than sintered LLZT with same composition. The electronic conductivity of LLZT film is six digits lower than Li^+ ion conductivity, demonstrating the dominant Li^+ ion conduction of LLZT film. In order to achieve higher Li^+ ion conductivity in solid electrolyte film formed by AD, further study is necessary to suppress the formation of the impurity phases in Li-stuffed garnet oxide solid electrolyte film, particularly by the powder treatment such as the composition, synthesis route, and controlling of the particle size.

Acknowledgements

This work was partly supported by Grant-in-Aid for Scientific Research (KAKENHI) Grant Numbers 26630111 and 16K06218 from the Japan Society for the Promotion of Science (JSPS), Japan, and also

supported by TOYOAKI Scholarship Foundation and Research Foundation for the Electro-technology of Chubu (R-28241).

Appendix A. Supplementary material

Supplementary data associated with this article can be found in the online version at <http://dx.doi.org/10.1016/j.pnsc.2017.06.002>.

References

- [1] K. Takada, *Acta Mater.* 61 (2013) 759–770.
- [2] M. Tatsumisago, M. Nagao, A. Hayashi, *J. Asian Ceram. Soc.* 1 (2013) 17–25.
- [3] S. Teng, J. Tan, A. Tiwari, *Curr. Opin. Solid State Mater. Sci.* 18 (2014) 29–38.
- [4] Y. Ren, K. Chen, R. Chen, T. Liu, Y. Zhang, C.W. Nan, *J. Am. Ceram. Soc.* (2015) 1–21.
- [5] R. Murugan, V. Thangadurai, W. Weppner, *Angew. Chem. Int. Ed.* 46 (2007) 7778–7781.
- [6] J. Awaka, N. Kijima, H. Hayakawa, J. Akimoto, *J. Solid State Chem.* 182 (2012) 2046–2052.
- [7] J. Awaka, A. Takashima, K. Kataoka, N. Kijima, Y. Idemoto, *J. Akimoto, Chem. Lett.* 40 (2011) 60–62.
- [8] C.A. Geiger, E. Alekseev, B. Lazic, M. Fisch, T. Armbruster, R. Langner, M. Fechtelkord, N. Kim, T. Pettko, W. Weppner, *Inorg. Chem.* 50 (2011) 1089–1097.
- [9] M. Kotobuki, K. Kanamura, Y. Sato, T. Yoshida, *J. Power Sources* 196 (2011) 7750–7754.
- [10] S. Kumazaki, Y. Iriyama, K.H. Kim, R. Murugan, K. Tanabe, K. Yamamoto, T. Hirayama, Z. Ogumi, *Electrochem. Commun.* 13 (2011) 509–512.
- [11] E. Rangasamy, J. Wolfenstein, J. Sakamoto, *Solid State Ion.* 206 (2012) 28–32.
- [12] Y. Li, J. Han, C. Wang, S.C. Vogel, H. Xie, M. Xu, J.B. Goodenough, *J. Power Sources* 209 (2012) 278–281.
- [13] S. Ohta, T. Kobayashi, *J. Power Sources* 196 (2011) 3342–3345.
- [14] Y. Li, J. Han, C. Wang, H. Xie, J.B. Goodenough, *J. Mater. Chem.* 22 (2012) 15357–15361.
- [15] A. Logéat, T. Köhler, U. Eisele, B. Stiaszny, A. Harzer, M. Tovar, A. Senyshyn, H. Ehrenberg, B. Kozinsky, *Solid State Ion.* 206 (2012) 33–38.
- [16] H. Buschmann, S. Berendts, B. Mogwitz, J. Janek, *J. Power Sources* 206 (2012) 236–244.
- [17] Y. Wang, W. Lai, *Electrochem. Solid State Lett.* 15 (2012) A68–A71.
- [18] R. Inada, K. Kusakabe, T. Tanaka, S. Kudo, Y. Sakurai, *Solid State Ion.* 262 (2014) 568–572.
- [19] J. Tan, A. Tiwari, *ECS Solid State Lett.* 1 (2012) 957–960.
- [20] S. Kim, M. Hirayama, S. Taminato, R. Kanno, *Dalton Trans.* 42 (2013) 13112–13117.
- [21] D.J. Kalita, S.H. Lee, K.S. Lee, D.H. Ko, Y.S. Yoon, *Solid State Ion.* 229 (2012) 14–19.
- [22] K. Tadanaga, H. Egawa, A. Hayashi, M. Tatsumisago, J. Mosa, M. Aparicio, A. Duran, *J. Power Sources* 273 (2015) 844–847.
- [23] J. Akedo, *J. Am. Ceram. Soc.* 89 (2006) 1834–1839.
- [24] J. Akedo, M. Lebedev, *Appl. Phys. Lett.* 77 (2000) 1710–1712.
- [25] J.H. Ryu, J.J. Choi, B.D. Hahn, D.S. Park, W.H. Yoon, K.-H. Kim, *Appl. Phys. Lett.* 90 (2007) 152901.
- [26] W.H. Yoon, J. Ryu, J.J. Choi, B.D. Hahn, J.H. Choi, B.K. Lee, J.H. Cho, D.S. Park, *J. Am. Ceram. Soc.* 93 (2010) 2125–2127.
- [27] H. Usui, M. Shibata, K. Nakai, H. Sakaguchi, *J. Power Sources* 196 (2011) 2143–2148.
- [28] S. Takai, H. Sakaguchi, K. Tanaka, Y. Nagao, T. Esaka, *Electrochemistry* 76 (2008) 293–296.
- [29] I. Kim, J. Park, T.-H. Nam, K.-W. Kim, J.-H. Ahn, D.-S. Park, C. Ahn, G. Wang, H.-J. Ahn, *J. Power Sources* 244 (2013) 646–651.
- [30] S. Iwasaki, T. Hamanaka, T. Yamakawa, W.C. West, K. Yamamoto, M. Motoyama, T. Hirayama, Y. Iriyama, *J. Power Sources* 272 (2014) 1086–1090.
- [31] R. Inada, K. Shibukawa, C. Masada, Y. Nakanishi, Y. Sakurai, *J. Power Sources* 253 (2014) 181–186.
- [32] C.W. Ahn, J.J. Choi, J. Ryu, B.D. Hahn, J.W. Kim, W.H. Yoon, J.H. Choi, D.S. Park, *J. Power Sources* 273 (2015) 336–340.
- [33] C.-W. Ahn, J.-J. Choi, J. Ryu, B.-D. Han, J.-W. Kim, W.-H. Yoon, J.-H. Choi, D.-S. Park, *Carbon* 82 (2015) 135–142.
- [34] D. Popovici, H. Nagai, S. Fujisima, J. Akedo, *J. Am. Ceram. Soc.* 94 (2011) 3847–3850.
- [35] R. Inada, K. Ishida, M. Tojo, T. Okada, T. Tojo, Y. Sakurai, *Ceram. Int.* 41 (2015) 11136–11142.
- [36] C.W. Ahn, J.J. Choi, J. Ryu, B.D. Hahn, J.W. Kim, W.H. Yoon, J.H. Choi, D.S. Park, *J. Electrochem. Soc.* 162 (2015) A60–A63.
- [37] H. Nemori, Y. Matsuda, S. Mitsuoka, M. Matsui, O. Yamamoto, Y. Takeda, N. Imanishi, *Solid State Ion.* 282 (2015) 7–12.
- [38] Y. Kim, A. Yoo, R. Schmidt, A. Sharafi, H. Lee, J. Wolfenstein, J. Sakamoto, *Front. Energy Res.* 4 (2016) 20.
- [39] R. Inada, S. Yasuda, M. Tojo, K. Tsuritani, T. Tojo, Y. Sakurai, *Front. Energy Res.* 4 (2016) 28.
- [40] I. Kokal, M. Somer, P.H.L. Notten, H.T. Hintzen, *Solid State Ion.* 185 (2011) 42–46.
- [41] M. Matsui, K. Sakamoto, K. Takahashi, A. Hirano, Y. Takeda, O. Yamamoto, N. Imanishi, *Solid State Ion.* 262 (2014) 155–159.